2D MoS2/BiOBr van der Waals heterojunctions by liquid-phase exfoliation as photoelectrocatalysts for hydrogen evolution

ARTICLE

Received 00th January 20xx,
Accepted 00th January 20xx

DOI: 10.1039/x0xx00000x

2D MoS_2/BiOBr van der Waals heterojunctions by liquid-phase exfoliation as photoelectrocatalysts for hydrogen evolution

Mengjiao Wang,*[a] Silvio Osella,[b] Rosaria Brescia,[c] Zheming Liu,[d] Jaime Gallego,[a] Mattia Cattelan,[e] Matteo Crisci,[a] Stefano Agnoli[e] and Teresa Gatti*[a,f]

As a semiconductor used for the photocatalytic hydrogen evolution reaction (HER), BiOBr has received intensive attention in recent years. However, the high recombination of photoexcited charge carriers results in poor photocatalytic efficiency. The combination with other photoactive semiconductors might represent a valuable approach to deal with these intrinsic limitations of the material. Given that BiOBr has a 2D structure, we propose a simple liquid-phase exfoliation method to peel BiOBr microspheres into few-layers nanosheets. By tuning the weight ratio between the precursors, we prepare a series of 2D MoS_2/BiOBr van der Waals (vdW) heterojunctions and study their behaviour as (photo)electrocatalysts for the HER, finding dramatic differences as a function of weight composition. Moreover, we evidence that pristine 2D BiOBr and the heterojunctions, with the exception of the 1% MoS_2/BiOBr composition, each undergoes photocorrosion, with BiOBr being reduced to metallic Bi. These findings represent useful guidelines to design of novel 2D material-based (photo)electrocatalysts for the production of sustainable fuels.

1. Introduction

Photoelectrocatalytic (PEC) hydrogen evolution is a valuable process that allows storing solar light and electrical energy into a portable and clean fuel like H_2. In this combined method, the energy conversion efficiency is supposed to be higher than that of single photocatalysis and electrocatalysis.[1] A variety of inorganic oxides and chalcogenides have been applied as photoelectrocatalysts in the hydrogen evolution reaction, such as Cu_2O[2], $BiVO_4$[3], Fe_2O_3[4], Sb_2Se_3[5], MoS_2[6], CdS[7] and many others. However, the efficiency and the stability of the catalysts in these PEC systems still remain open issues. Particularly, a fast charge recombination results in a low utilization of the photogenerated charge carriers.[8-9] Moreover, photocatalysts and photoelectrocatalysts suffer from photocorrosion: in oxides such as Cu_2O the photo-generated electrons and holes change the chemical structure of the catalyst instead of reacting with H_2O.[10–12] Therefore, the discovery of more efficient and stable photoelectrocatalysts is one of the most important directions in the field of hydrogen production.

BiOBr is emerging as an interesting photocatalyst because of its unique internal electric field and band structure, which facilitate the separation and mobility of the charge carriers. Moreover, the layered structure, kept together by van der Waals (vdW) interactions, makes BiOBr suitable for exfoliation into 2D nanosheets, with high surface area available for catalytic reactions. There are already a number of published works studying the photocatalytic processes promoted by 2D BiOBr, such as the photodegradation of pollutants[13–15], photoreduction of CO_2[16], photocatalytic nitrogen fixation[17] and photocatalytic water splitting.[18] However, like most of the photocatalysts that are still at the laboratory stage development, 2D BiOBr is in its research infancy as well. The application of an additional voltage to drive the catalytic reaction increases the efficiency of photoreactions, but the stability of BiOBr in the PEC environment can be strongly compromised. Originally, 2D BiOBr was used as a photoanode to produce O_2 during water splitting, mainly because the energy

[a] Institute of Physical Chemistry and Center for Materials Research (LaMa), Justus Liebig University, 35392 Giessen, Germany. E-mail: mengjiao.wang@phys.chemie.uni-giessen.de
[b] Chemical and Biological Systems Simulation Lab, Centre of New Technologies, University of Warsaw, 02097 Warsaw, Poland.
[c] Electron Microscopy Facility, Istituto Italiano di Tecnologia, Via Morego, 30, 16163 Genova, Italy.
[d] Nanochemistry Department, Istituto Italiano di Tecnologia, 16163 Genova, Italy.
[e] Department of Chemical Sciences, University of Padova, 35131 Padova, Italy.
[f] Department of Applied Science and Technology, Politecnico di Torino, 10129 Torino, Italy. E-mail: teresa.gatti@polito.it

†Electronic Supplementary Information (ESI) available: [details of any supplementary information available should be included here]. See DOI: 10.1039/x0xx00000x

position of its valence band (VB) energy is suitable for water oxidation, while the conduction band (CB) is not properly positioned for the reduction of H^+/H_2.[19] However, recently a growing number of reports describes BiOBr-based photocathodes as photoelectrocatalysts for the hydrogen evolution reaction (HER). In this contest, different methods have been applied to tune the band structure of BiOBr to increase the PEC efficiency. For example, Shi et al. synthesized facet-dependent BiOBr and found that samples with dominating (001) facets have a band structure that is appropriate for proton reduction and performs excellent HER.[18] Wang et al. applied a chemical vapor deposition method to grow 2D BiOBr for PEC HER.[20] Despite its promising catalytic activity, the photoreduction of BiOBr to metallic Bi remains a bottleneck to overcome to maintain the catalyst stability.[19] Different strategies have been applied to enhance both efficiency and stability of BiOBr. Among them, the generation of heterojunctions (HJs) with other materials was particularly effective and various examples are present in the literature. Theoretically, a HJ establishing a fine-tuned internal electric field is helpful to separate and transfer the photogenerated electrons or holes from the original photoelectrocatalyst, in order to reduce the charge recombination and hinder the photocorrosion reaction. Li et al. reported an oxygen vacancy-BiOBr/$Cu_{2-x}S$ type I HJ with high hydrogen evolution rate, in which the divalent defects in the HJ are able to create interfacial polarization, and this polarization has a synergetic effect with the internal electric field.[21] This work indeed inspired us to fabricate 2D BiOBr HJs with other materials, to further explore the potential of this approach to boost PEC HER efficiency and stability in this catalyst.

The design of vdW HJs has been pioneered by combining different 2D layered materials through facile synthesis methods.[22] The construction of vdW bonds has already proved to be a promising technique for boosting the catalytic property of 2D materials.[23] MoS_2 is a popular 2D layered material used for building vdW HJs with other layered materials.[24] These vdW HJs, such as black phosphorus/MoS_2[25], graphene/MoS_2[26], WSe_2/MoS_2[27] and $MoS_2/MoSe_2$,[28] can provide access to variable bandgaps, fast charge carrier transport or interfacial coupling effects. There are several works reporting on MoS_2/BiOBr HJs, and a variety of synthesis methods such as mechanical ball milling[29], chemical deposition[30] and wet chemical co-precipitation method[31] have been applied to fabricate similar nanoarchitectures with different morphologies. These materials have been mainly applied in photocatalytic degradation of pollutants, but the analyses on the band structure and type of HJ present in these systems show significant discrepancies, thus the photocatalytic mechanism is still unclear. Moreover, to the best of our knowledge, a 2D MoS_2/BiOBr vdW HJ has not been reported yet.

Therefore, in this work, we used a solvothermal route to prepare BiOBr microspheres, and the liquid-phase exfoliation (LPE) to pre-treat a bulk MoS_2 powder. Then, we employed another LPE process on the mixture of BiOBr microspheres and pre-treated MoS_2 to obtain 2D BiOBr/MoS_2 vdW HJs (Scheme 1). The products, with different MoS_2/BiOBr ratios, were tested

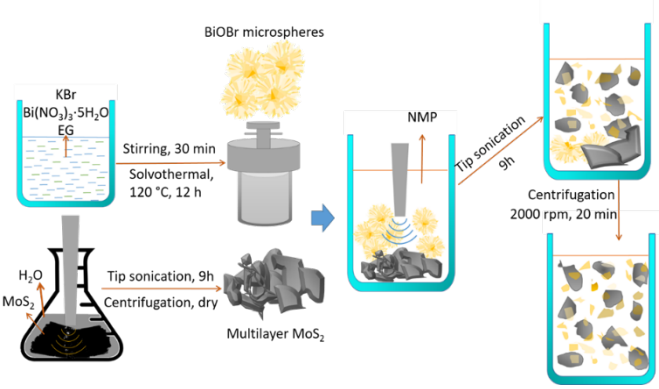

Scheme 1 Sketch of the process employed in this work to synthesize 2D MoS_2/BiOBr HJs. Solvothermal and LPE methods have been applied to yield inks of the layered binary nanostructure in NMP.

in the PEC HER. Surprisingly, only the 1% (w/w) MoS_2/BiOBr HJ has a remarkable catalytic activity among all investigated samples. In this system, during PEC, BiOBr absorbs the UV radiation and generates separated electrons and holes, while MoS_2 accepts the photogenerated electrons and performs the HER, while avoiding BiOBr photocorrosion at the same time. Our findings provide a novel method for synthesizing MoS_2/BiOBr vdW HJs and a new strategy to modify the efficiency and stability of 2D materials-based photoelectrocatalysts.

2. Results and discussion

To produce the 2D MoS_2/BiOBr HJs, the two precursors, namely BiOBr microspheres and layered MoS_2, were prepared by the solvothermal and LPE methods, respectively. The structural and morphological characterizations of these intermediates are shown in Fig. S1 of the Supporting Information (S.I.). Then, a series of HJs with different MoS_2/BiOBr ratios were synthesized (Scheme 1) as described in detail in the Experimental Section, and the samples were labelled according to the weight ratio of MoS_2, namely 1% MoS_2/BiOBr, 5% MoS_2/BiOBr, 10% MoS_2/BiOBr and 50% MoS_2/BiOBr. The pure 2D layered BiOBr and MoS_2 were synthesized by LPE for comparison as well. The weight ratio of MoS_2 in the resulting HJs was determined through energy dispersive X-ray spectroscopy (EDX) on a scanning electron microscope (SEM) (see Fig. S2 and Table S1) except for 1% MoS_2/BiOBr, of which the weight ratio was quantified by X-ray photoelectron spectroscopy (XPS) (see Fig. S3 and Table S1). Moreover, the unbalanced stoichiometry of Bi/Br/O indicates a damage of bulk BiOBr, which proves the formation of layered structure of BiOBr indirectly.[32] SEM images provide a general view of the morphology of all the samples (see Fig. S4). It is clear that the BiOBr spheres are completely deconstructed into separated microsheets by the mechanic force from LPE method, and all the samples are micro-/nano-sheets with irregular shape. Bright-field transmission electron microscopy (BF-TEM) images (Fig. 1a and 1f) reveal that pure 2D BiOBr sheets have a size distribution between 50 and 150 nm, while 2D MoS_2 sheets have an average size of more than 500 nm. This is supported by high-angle annular dark field scanning transmission electron microscopy (HAADF-STEM) and STEM-

EDX analyses on one of the composite materials (Fig. S5 and S6), which clearly show that lower-contrast, extended objects in the composites can be identified as MoS_2 sheets, while higher-contrast, less extended objects are BiOBr NPLs. Fig. 1b-e show the morphology of 1% MoS_2/BiOBr, 5% MoS_2/BiOBr, 10% MoS_2/BiOBr and 50% MoS_2/BiOBr, respectively, highlighting the close connection between the two components. Further characterization has been carried out through STEM-EDX mapping, revealing a clear overlapping of Mo and Bi distribution in some areas (Fig. 1g). Fig. 1i is a high-resolution TEM (HRTEM) image from a region in Fig. 1h. The small nanosheet can be attributed to the tetragonal BiOBr phase (ICSD number: 61225), with a [111] orientation (see the corresponding fast Fourier transformation in Fig. 1j). This BiOBr nanosheet overlaps on a distorted [001]-oriented hexagonal MoS_2 sheet (ICSD number: 95569). This demonstrates the formation of HJs between MoS_2 and BiOBr. However, as the MoS_2 (001) is not totally flat in the HRTEM, it is possible that the smaller BiOBr flakes show a distorted orientation that is different from the facet of the HJ interface. Therefore, it is difficult to conclude that the vdW HJ is formed by BiOBr (111) plane and MoS_2 (001) plane.

The powder X-ray diffraction (P-XRD) patterns of 2D BiOBr and 2D MoS_2 reveal the presence of the tetragonal BiOBr phase (ICSD number: 61225) and hexagonal MoS_2 phase (ICSD number: 95569) without any impurities (Fig. 2a). Except for the 1% MoS_2/BiOBr sample, which has a low MoS_2 content and displays only the BiOBr structure, the P-XRD patterns of the MoS_2/BiOBr HJs feature both phases with an increasing peak intensity ratio MoS_2 (002) (located at 14.4°) to BiOBr (102) (located at 31.7°) when the weight ratio of MoS_2 increases. This is because the XRD peak intensity at 14.4° is related to the extended (001) planes in MoS_2 2D sheets, which increases because of the increasing amount of MoS_2 component. It is worthy to mention that the characteristic peak appeared at 10.4°, which is corresponding to (001) direction of tetragonal BiOBr phase, is not clearly detected in BiOBr precursor or LPE 2D BiOBr, while it is detected in the four HJ samples. This can be due to the fact that the combination with MoS_2 enhances the

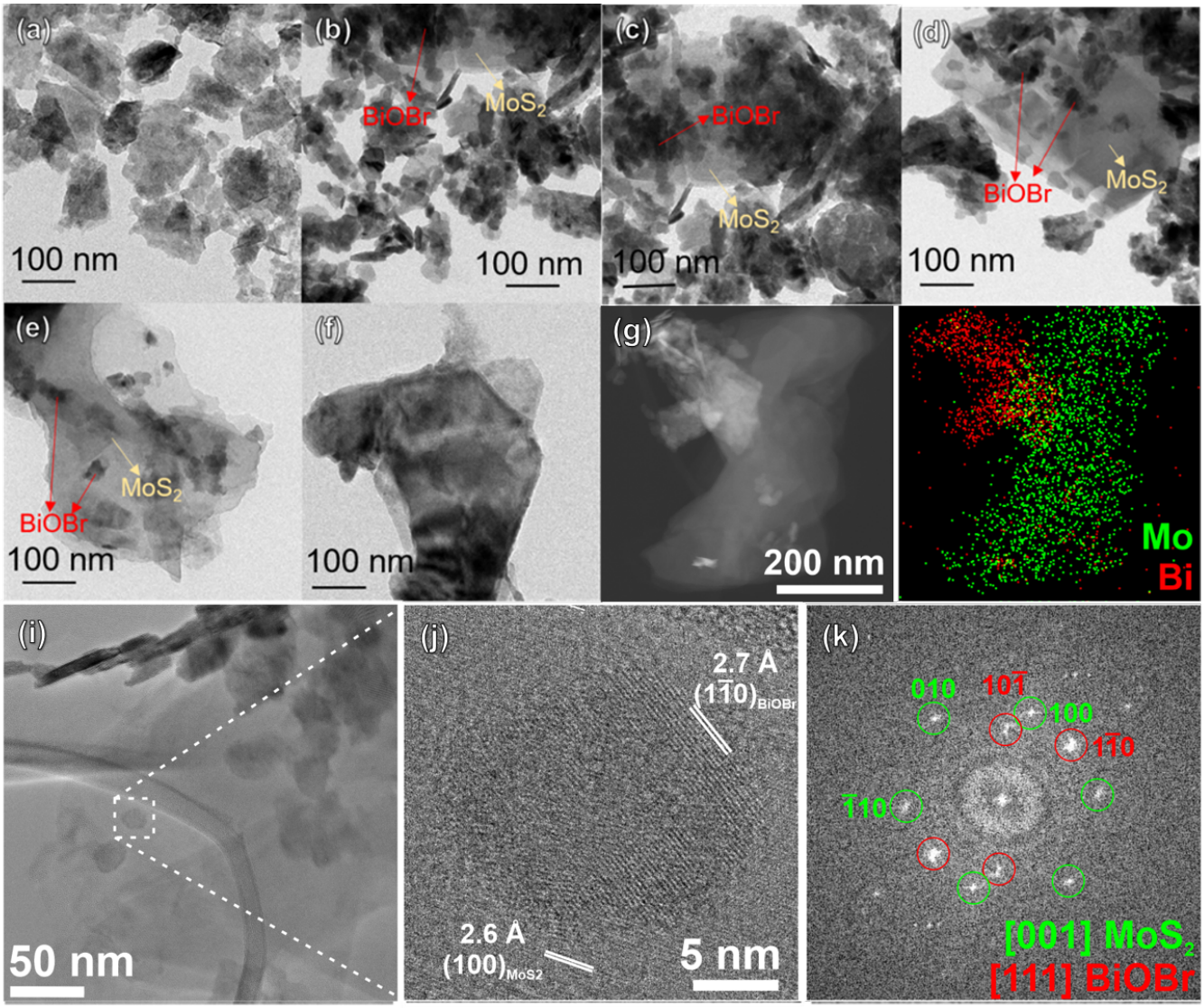

Fig. 1 BF-TEM images of (a) LPE BiOBr, (b) 1% MoS_2/BiOBr, (c) 5% MoS_2/BiOBr, (d) 10% MoS_2/BiOBr, (e) 50% MoS_2/BiOBr and (f) LPE MoS_2. (g) HAADF image and (h) EDX elemental mapping over the generic HJ sample, (i) HRTEM image of a HJ and (j) corresponding fast Fourier transform image of region (i).

stacking of BiOBr layers along (001) direction. Raman spectra were also recorded to identify possible vdW interactions between BiOBr and MoS_2. The characteristic peaks of both components were distinguished in all the HJs (Fig. 2b). Specifically, the peaks at 113.2 and 160.6 cm^{-1} correspond to the A_{1g} and E_g mode of internal Bi–Br stretching, respectively, while the peaks at around 381.3 and 405 cm^{-1} correspond to the in-plane (E_{2g}) mode of Mo-S and out-of-plane (A_{1g}) mode of S-S.[33] Clearly, the intensity of BiOBr characteristic peaks is reduced dramatically with the progressive increase in MoS_2 content, indicating a strong interaction between the two components. As for the two characteristic peaks of MoS_2, a shift to higher wavenumbers for both peaks is observed for the HJs compared to 2D MoS_2, further pointing out a possible vdW connection between MoS_2 and BiOBr. To analyse the characteristic peaks of MoS_2 better, we show a magnification of the region between 360 and 430 cm^{-1} in Fig. 2c. It is reported that the distance between the two fingerprint peaks (E_{2g} and A_g) of MoS_2 has a strong correlation with the number of layers.[34–36] As for the bare LPE MoS_2, we find a wavenumber difference of 24.3 cm^{-1}, indicating that an average number of layers in the sample around 3. On the other hand, for all the here presented HJs, an observed wavenumber difference of over 25 cm^{-1} between the two representative peaks probably indicates an increased number of MoS_2 layers. However, this accumulation of layers can be attributed both to MoS_2-MoS_2 layer restacking and MoS_2-BiOBr restacking, with the second effect being predominant at lower MoS_2 concentration in the HJs due to the higher probability for a MoS_2 sheet to interact with a BiOBr layer. This is also indirectly proved by the wavenumber shift of both peaks. It is known that the Raman peak energy is strongly related to the polarization of the constituent atoms in the phonon vibration, with bonds involving softer atoms requiring lower energies to vibrate. Since oxygen is largely present in BiOBr (the O/Bi atomic ratio is more than 1, see Table S1), it is possible that oxygen atoms located at the interface of the HJ interact with sulphur vacancies on MoS_2, thus causing an average decrease in polarizability in the Mo-S(O) and S-S(O) bonds (due to the harder character of O compared to S), that drives the frequency shift to higher wavenumbers, as it was also observed for *in-situ* oxygen-doped MoS_2 monolayers.[37]

UV-visible absorption spectra (Fig. 3a-b) allow to estimate the light-harvesting features and, by applying the Tauc method, also the band gaps of the LPE HJs. As expected, both 2D BiOBr (3.15 eV) and 2D MoS_2 (1.75 eV) show wider band gaps compared to their corresponding bulk material precursors.[38, 39] In addition, the band gap of the vdW HJs progressively narrows with the addition of MoS_2, from 3.01 eV to 2.25 eV (see details in Table S2).[40, 41] Photoluminescence (PL) spectra were also measured at an excitation wavelength of 375 nm, which was determined to be the wavelength providing higher PL intensity by recording the excitation spectrum of bare 2D BiOBr (Fig. S7). As shown in Fig. 3c, both 2D BiOBr and the HJs feature a broad emission, with a peak located at around 451.7 nm for pure 2D BiOBr and 477.7 nm for the HJs. Considering that a large Stokes shift (~ 0.4 eV) is present between the absorption peak (3.15 eV) and the PL emission (2.74 eV), it is safe to assume that this PL generates from an exciton emission related to the defects and surface oxygen vacancy of 2D BiOBr.[42] Besides, the absence of the band edge emission, which should be at around 400 nm, suggests a weak recombination of photogenerated charges inside 2D BiOBr. However, the intensity of PL decreases with the increasing content of 2D MoS_2, which is an important signature that the optical recombination path in 2D BiOBr is strongly influenced by the presence of the nearby MoS_2 nanosheets.

To gain further insight into the electronic properties of the HJs constructed by different ratios of MoS_2 and BiOBr, density functional theory (DFT) calculations were performed on three simplified HJ models by tuning the layer ratios of MoS_2 and BiOBr, namely 1 layer of MoS_2 and 2 layers of BiOBr (1-MoS_2/2-BiOBr), 1 layer of MoS_2 and 1 layer of BiOBr (1-MoS_2/1-BiOBr), and 2 layers of MoS_2 and 1 layer of BiOBr (2-MoS_2/1-BiOBr). The optimized structures of the three different interfaces are reported in Fig. 4a, S6a and S6c. As it can be clearly identified in all of them, the BiOBr sheet always exposes the oxygen-rich face towards the interface with MoS_2 and not towards the bromine-rich one. This further corroborates the previously discussed observations on Raman features of MoS_2 in the HJs. Our calculations further suggest that the band structure and charge transfer are influenced by different layer combinations. From the total and partial density of state (DOS) analysis of the different interfaces we can observe a prevalent MoS_2 character

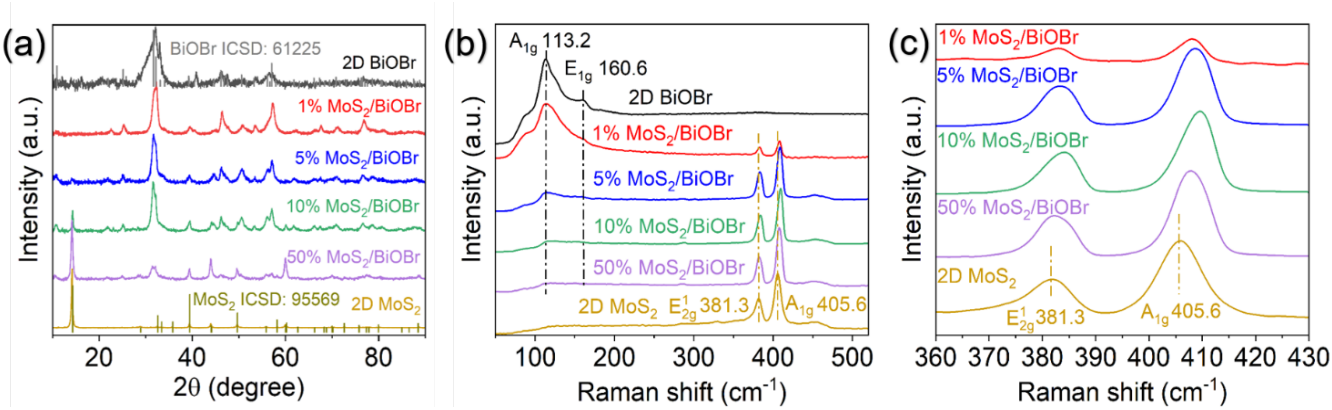

Fig. 2 (a) XRD patterns of the MoS_2/BiOBr HJs. The bulk reflexes of tetragonal BiOBr (ICSD number: 61225) and hexagonal MoS_2 (ICSD number: 95569) are also reported for the sake of clarity, by means of grey and brown bars, respectively. (b) Raman spectra of the MoS_2/BiOBr HJs. (c) Magnification of the Raman spectra of the HJs and 2D MoS_2 in the range 360- 430 cm^{-1}.

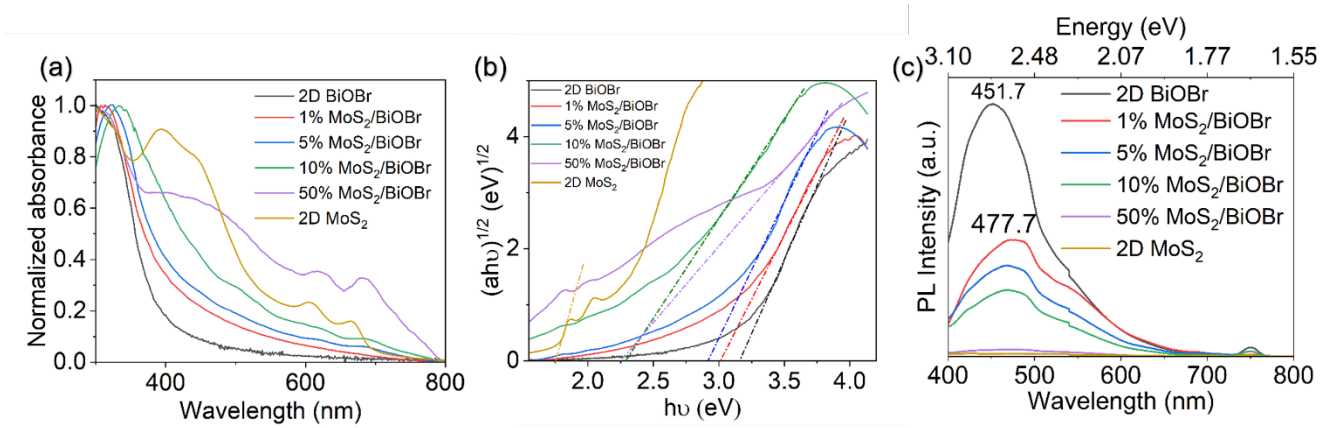

Fig. 3 (a) Absorption spectra (b) Tauc plot and (c) PL spectra of 2D BiOBr, 2D MoS_2 and the HJs.

for the valence band in all the three models, while for the valence band (VB) differences arise depending on the layer ratio difference (Fig. 4b, Fig. S8b and Fig.S8d). In particular, only for the 1-MoS_2/1-BiOBr HJ the VB is fully localized on the BiOBr, while for the other two interfaces mixed contributions arising from both MoS_2 and BiOBr are present, confirming the strong charge recombination effect that the presence of MoS_2 has on the overall electronic properties of the interface. In addition, the charge transfer analysis reveals that an almost constant amount of ~ 0.35 electrons is transferred from BiOBr to MoS_2, independently of the interface composition.

In agreement with optical analysis and DFT calculations, for the MoS_2/BiOBr HJ we can derive the energy diagram illustrated in Fig. 4c. In pure 2D BiOBr, the photogenerated electrons recombine with the holes trapped by the defects and oxygen vacancies through photon emission. However, in the MoS_2/BiOBr HJs, the VB depends on the layer ratio of the two contents according to our calculation. The HJ consisting of 1 layer of MoS_2 and 1 layer of BiOBr has a fully localized VB over BiOBr, thus allowing the photogenerated holes to move to MoS_2; while in the other two combinations, the VB is shared between MoS_2 and BiOBr, which means the photogenerated holes are possibly dispersed both in MoS_2 and BiOBr, and the amount of transferred holes from BiOBr to MoS_2 is dependent on the ratio of MoS_2. The DFT calculations prove that the holes photogenerated in BiOBr can remain in BiOBr or be partially transferred on the surface of MoS_2. On the other hand, the lower conduction band minimum (CBM) of MoS_2 allows the photoexcited electrons to transfer from BiOBr to MoS_2. Overall, the system can be considered a Type-I HJ, in which a formal energy transfer (ET) process takes place from BiOBr to MoS_2 following photo-excitation of the former through a charge exchange mechanism. Therefore, the charge recombination can proceed through two paths: the electron-hole recombination between the CBM and VBM of MoS_2 or the recombination between the CBM of MoS_2 and defects or oxygen vacancies on BiOBr (see the brown solid lines in Fig. 4c). As the amount of MoS_2 is increased in the HJs, increasing amounts of excited electrons recombine with the holes inside MoS_2, meanwhile the charges for the BiOBr-centred trap-assisted recombination are reduced.

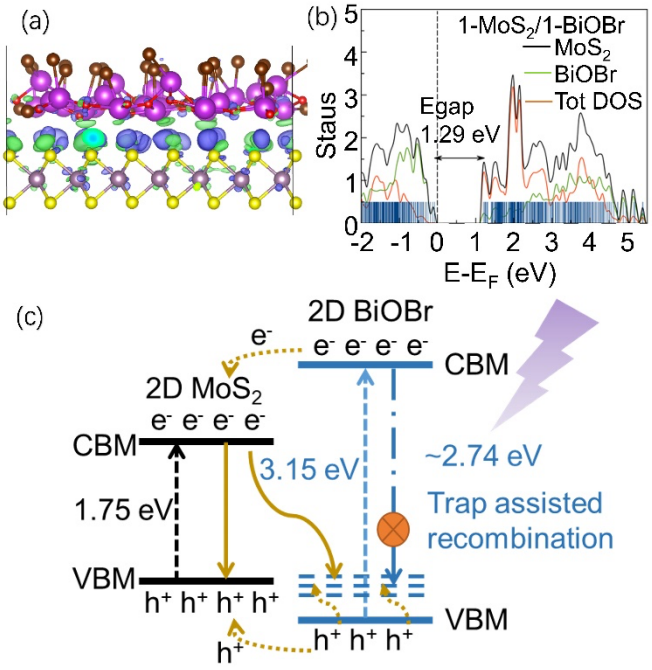

Fig. 4 (a) Optimized structures and charge difference analyses for 1-MoS_2/1-BiOBr. The MoS_2/BiOBr interlayer distance is measured in the 0.270-0.292 nm window depending on the number of layers present. The atoms are represented with the following colors; yellow: sulfur, gray: molybdenum, red: oxygen, purple: bismuth, brown: bromine. Blue surface represents negative charge; green surface the positive charge. (b) Total and partial DOS analyses for 1-MoS_2/1-BiOBr and. The Fermi energy is set to zero (dotted line), blue vertical lines show the eigenvalues of the interface. (c) Schematic illustration of the photoexcitation dynamics in the 2D BiOBr/MoS_2 HJs .

The PEC HER performance of the prepared MoS_2/BiOBr HJs was studied through linear sweep voltammetry (LSV) in neutral pH conditions (see the Experimental section for details). Acidic and basic conditions were not tested due to the pronounced instability of BiOBr in these media.[43,44] The resulting polarization curves are reported in Fig. 5a. Before each LSV curve was collected, 5 cycles of cyclic voltammetry with a scan rate of 50 mV/s over the 0.2~-0.6 V vs. RHE were performed in order to obtain a stabilized curve (Fig. S9). From these curves it is evident that in dark, the EC properties heavily depend on the composition of the HJs (dash dot curves). The addition of MoS_2 nanosheets helps to decrease the onset potential systematically

from ~-524 mV to ~0 mV going from the pure 2D BiOBr to 10% MoS_2/BiOBr. The kinetics of HER of different samples is compared by the Tafel slope, which is estimated from the polarization curves. As shown in Fig. 5b, the Tafel slopes of 2D BiOBr, 1% MoS_2/BiOBr, 5% MoS_2/BiOBr, 10% MoS_2/BiOBr and 50% MoS_2/BiOBr increase from ~126 mV/dec to ~245 mV/dec, except for the 1% MoS_2/BiOBr HJ, with a value higher than that found for 5% MoS_2/BiOBr (see Table 1 for specific values). 2D MoS_2, which is here produced in its thermodynamically stable phase, i.e. the semiconducting H-phase, does not activate HER in the bias range of 0/-0.6 V vs RHE, thus no Tafel slope is calculated. However, the PEC HER of these samples shows different trends from the EC HER (solid curves). The onset potential decreases from ~-448 mV for 2D BiOBr to ~281 mV for 1% MoS_2/BiOBr, while it increases again when the weight ratio of MoS_2 gets to 5%. From these data, it is apparent that the PEC HER performance is enhanced with respect to standard EC only for 2D BiOBr and the 1% MoS_2/BiOBr HJ, while the performance in PEC HER of 5% MoS_2/BiOBr, 10% MoS_2/BiOBr, 50% MoS_2/BiOBr and 2D MoS_2 is not better than the corresponding EC HER. The onset potential for the 10% MoS_2/BiOBr HJ is even increased from ~0 V to ~-336 mV, strongly indicating that light energy is not helpful to improve the HER activity in this sample. However, this unhelpful influence of UV light is probably due to the occurrence of a chemical transformation of the samples under UV irradiation, which can be deduced from the irreversible redox peaks in the initial CV curves (Fig. S9).

The influence of the light source on the kinetics of the reactions results to be also different on samples with different compositions. In Table 1, useful to compare the values for each sample under EC and PEC condition, it is found that the Tafel slope is increased for both 2D BiOBr and 1% MoS_2/BiOBr HJ, while decreased for 10% MoS_2/BiOBr and 50% MoS_2/BiOBr HJs. This indicates that the influence of UV illumination on the kinetics of HER is different, depending on the composition of the samples. Moreover, the redox peaks that appear in these last samples in the range -0.2/0.1 V are possibly ascribed to the reduction peak of Bi^{III} to Bi^0.[45] The photocurrent density–voltage curves of 2D BiOBr, 1% MoS_2/BiOBr and 5% MoS_2/BiOBr are shown in Fig. 5a. The photocurrent density of pure 2D BiOBr reaches 1.0 mA/cm² at -0.6 V vs. RHE. 1% MoS2/BiOBr exhibits a noticeable enhanced photocurrent density of 1.9 mA/cm² at -0.54 V vs. RHE, then reduced to 1.5 mA/cm2 at -0.6 V vs. RHE. This is mainly because of a sluggish kinetic under the influence of the UV light source. Moreover, 1% MoS_2/BiOBr shows an earlier start of the reaction under illumination compared to 2D BiOBr. However, the photocurrent is barely detected in the 5% MoS_2/BiOBr or HJs with higher ratio of MoS_2.

Fig. 5d shows the transient photocurrent densities of the samples at open circuit voltage. An enhancement of electron–hole separation for the 1% MoS_2/BiOBr HJ is further confirmed by the increased photocurrent. Besides, a general photocurrent decay is observed in the three samples as well. The photocurrent of 2D BiOBr and 5% MoS_2/BiOBr is negligible after two on/off light cycles, while 1% MoS_2/BiOBr still shows around 1 μA/cm² of photocurrent density after three cycles. These results reflect a better stability of the 1% MoS_2/BiOBr HJ compared to the other samples.

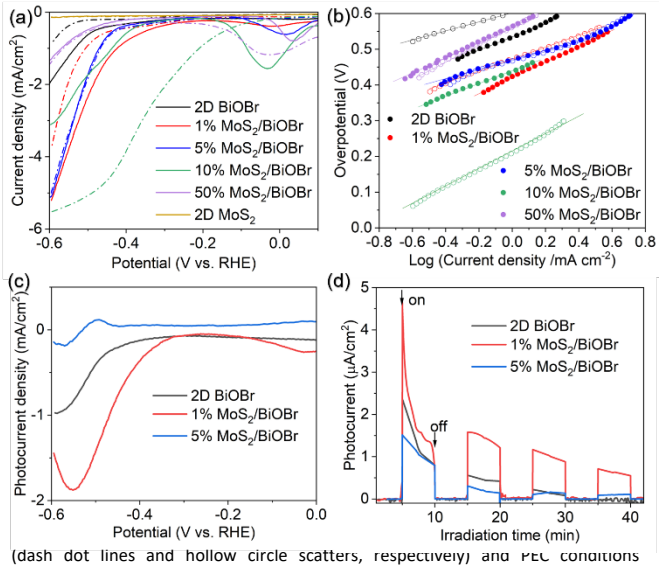

(dash dot lines and hollow circle scatters, respectively) and PEC conditions promoted by UV-light illumination at 16 mW/cm² (solid lines and filled circles) in 0.5 M Na_2SO_4 electrolyte medium. (c) Photocurrent density versus potential curves. (d) Transient photocurrent density as a function of time.

To further elucidate the mechanisms of PEC HER in the HJ samples, more characterizations were carried out on the aged electrodes to analyse their chemical and structural evolution. The samples after PEC HER were collected for P-XRD measurements. As shown in Fig. 6a, the phase structure of 2D BiOBr is changed from BiOBr to mainly metallic Bi (ICSD number 64703) with also a broad peak at around 28.3° (the yellow dash dot line), which is a characteristic peak belonging to Bi_2O_3 (ICSD number 27151, see Fig. S10). This result indicates that the BiOBr structure undergoes a chemical transformation: on one hand, the main part of Bi^{3+} is reduced to metallic Bi; on the other hand, Br is totally extracted during the PEC HER and part of the BiOBr is converted to Bi_2O_3. The BiOBr component in the HJs

Table 1. Summary of the HER parameters for 2D BiOBr and the MoS_2/BiOBr HJs.

Sample	Onset potential of EC HER (mV)	Onset potential of PEC HER (mV)	Tafel slope of EC HER (mV/dec)	Tafel slope of PEC HER (mV/dec)
2D BiOBr	-524	-448	126	185
1% MoS_2/BiOBr	-508	-281	155	210
5% MoS_2/BiOBr	-409	-402	133	131
10% MoS_2/BiOBr	0	-352	244	178
50% MoS_2/BiOBr	-336	-397	245	214

undergoes the same chemical transformation as 2D BiOBr except for the case of the 1% MoS_2/BiOBr HJ, which mainly maintains the original BiOBr structure with a very small amount of reduced Bi. In addition, in order to probe the different evolution of elemental composition and the surface chemical state in the HJs, the aged 1% MoS_2/BiOBr and 10% MoS_2/BiOBr HJs were chosen for high-resolution XPS analysis. Fig. 6b displays the Br 3d spectra. The 1% MoS_2/BiOBr HJ features the Br 3d peaks in the range from 67 eV to 70 eV, which is typical for Br in BiOBr.[46] On the other hand, no signal for the 10% MoS_2/BiOBr is detected, indicating the absence of Br on the surface of this electrode.[47] Meanwhile, the lack of Br in the EDS spectrum proves that no Br is found below the surface as well (see Fig. S11). The Bi 4f high-resolution XPS spectrum of 1% MoS_2/BiOBr shows two peaks of Bi $4f_{5/2}$ (164.5 eV) and Bi $4f_{7/2}$ (159.1 eV), which derive from the lattice Bi(III) ions in BiOBr (Fig. 6c). However, the corresponding Bi $4f_{5/2}$ and Bi $4f_{7/2}$ peaks shifted to 164.2 eV and 158.8 eV for 10% MoS_2/BiOBr. These shifts are likely due to the structure transformation from BiOBr to Bi_2O_3 in 10% MoS_2/BiOBr.[48] The existence of metallic Bi in 10% MoS_2/BiOBr is further visible from the weak shoulder peak at 156.8 eV in the signal of Bi $4f_{7/2}$. Since XPS can only probe chemical information within less than 10 nm of thickness of the sample, these results confirm that the surface of the 10% MoS_2/BiOBr electrode can form a layer of Bi_2O_3, while the dominant metallic Bi is mainly formed under the surface. The O 1s spectra are shown in Fig. 6d. 1% MoS_2/BiOBr after PEC HER shows two peaks near 529.9 and 531.3 eV, attributed to O in BiOBr and O in chemisorbed species, and one small shoulder near 533.1 eV from the O vacancies on the surface.[49-50] For the 10% MoS_2/BiOBr after PEC HER, the lattice O peak shift to 529.6 eV. This is explained by the chemical transformation from BiOBr to Bi_2O_3, which is in accordance with the XRD and Bi 4f XPS spectra. Besides, the other two peaks can be ascribed to different types of chemisorbed O, like –OH and H_2O.[51] Therefore, we believe that after PEC HER, the 1% MoS_2/BiOBr HJ is the only sample able to maintain the original structure with only a small amount of BiOBr reduced to metallic Bi. Indeed it is able to sustain at least 16 cycles of CV under UV light (Fig S9). On the other hand in the in 10% MoS_2/BiOBr HJ (and likely also in the other ones), most of the BiOBr is reduced to Bi(0), leaving a Bi_2O_3 layer covering the surface of the photoelectrode.

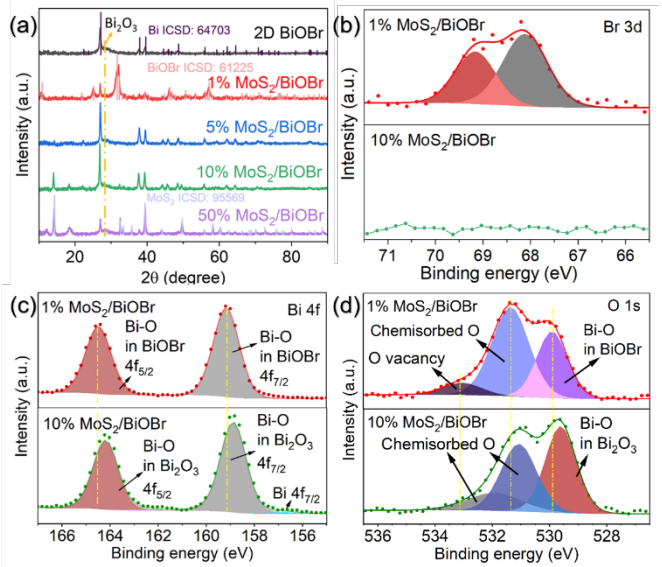

Fig. 6 (a) XRD of 2D BiOBr and the HJs after PEC HER. (b) Br 3d, (c) Bi 4f and (d) O 1s XPS spectra of 1% MoS_2/BiOBr and 10% MoS_2/BiOBr. All the samples were taken after 5 cycles of cyclic voltammetry of PEC HER with a scan rate of 50 mV/s.

Overall, the substantially different performance can be directly attributed to the different composition between the 2D materials. As evidenced by the XRD and XPS analysis on samples after PEC HER, different content of MoS_2 in the HJs results in different degree of reduction of BiOBr during the PEC process. Specifically, pristine 2D BiOBr is able to absorb UV light and to generate active species to boost the HER (see Fig. 5). However, this material is not stable under UV light because of the photoreduction from the photoelectrons. Our result is in accordance with the previous studies, which exhibited similar photocorrosion of 2D BiOBr. Superisingly, building vdW HJ with a low ratio of MoS_2 contributes to enhanced catalytic activity and structure stability, as proved in Fig. 5a, Fig. 6a and Fig. S12. The reason may be that enhanced electron density at the MoS_2/BiOBr interface is achieved due to the redistribution of charge density, which is highly favourable to electrochemical reduction reactions such as HER. Meanwhile, migration of extra photoelectrons to the conduction band of MoS_2 and the accumulation of photogenerated holes on the VB of BiOBr can prevent BiOBr from being reduced (see Fig. 4c). However, higher contents of MoS_2 in the HJs do not guarantee a better efficiency and stability. With a higher amount ratio of MoS_2 in the HJs, the assimilation of VBM of MoS_2 and BiOBr allows the transfer of more photoexcited holes to MoS_2, thus the extra electrons on BiOBr could facilitate the reduction of BiOBr (see Fig. S8c and S8d). Besides, as the oxygen vacancies on the surface of BiOBr are able to trap photoexcited electrons, the consumptions of these vacancies during the catalytic reaction might be another disadvantage to prevent BiOBr from photoreduction. As shown in Fig. S13 and 6d, oxygen vacancies are preserved during the PEC HER within the 1% MoS_2/BiOBr HJ but not within the 10% MoS_2/BiOBr one.

3. Conclusions

In summary, several 2D MoS_2/BiOBr vdW HJs with controllable compositions have been synthesized via a simple LPE method. These hybrid nanomaterials have been used as catalysts for EC and PEC HER, showing a dramatic difference in catalytic property and structural stability between different compositions. An enhancement in HER performance under UV illumination is found for pristine 2D BiOBr and the 1% MoS_2/BiOBr HJ, with the latter showing better catalytic performance and stability than the former. These excellent properties may be attributed to an optimal distribution of MoS_2 nanosheets among 2D BiOBr layers, which enables the chalcolcogenide to accept part of the active electrons from both the electric current and the light source. These charge transfer routes are favorable for protecting BiOBr from reducing to Bi and strengthen the stability of the catalyst. On the contrary, the positive influence of the photoexcitation is not effective when

the weight ratio of MoS_2 is above 5% in the HJs. The increasing ratio provides more possibilities for MoS_2 to accumulate in the HJ, which may prevent the above-mentioned charge transfer route and causes BiOBr to suffer from the presence of extra electrons accumulating on its surface. The present study and the novel methodology here described for the synthesis of 2D vdW HJs will contribute at enriching the fundamental knowledge in the field of 2D materials (photo)electrocatalysis and at inspiring new strategies for the design of more efficient and stable photoelectrocatalysts.

4. Experimental section

4.1 Materials

Bismuth(III) nitrate pentahydrate ($Bi(NO_3)_3•5H_2O$), Potassium bromide (KBr), ethylene glycol (EG), Molybdenum(IV) sulfide (MoS_2), N-Methyl-2-pyrrolidone (NMP), ethanol and Fluorine doped tin oxide (FTO) coated glass substrates were purchased from Sigma-Aldrich. Milli-Q water was obtained using the Milli-Q ultrapure system in all experiments.

4.2 Preparation of photoelectrocatalysts

$Bi(NO_3)_3•5H_2O$ and KBr were used as precursors to successfully synthesize BiOBr microspheres by a solvothermal method, which is modified from previous work of Shi et al.[52] Briefly, 83.3 mg of KBr was dissolved in 10 mL of EG, then 339.5 mg of $Bi(NO_3)_3•5H_2O$ was added into the solution and stirred for 30 min at room temperature, transferred into a 40 mL Teflon autoclave, and solvothermally treated at 120 °C for 12 h. After natural cooling, the white sample was collected and washed with ethanol and H_2O to remove unreacted chemicals and impurities. The structure and the morphology were determined by P-XRD and SEM, as shown in Fig. S1.

To synthesize the HJs, multilayer MoS_2 was firstly obtained by liquid phase exfoliation (LPE) with a tip-sonicator for 9 h using 500 mL of H_2O and 5 g of MoS_2 powder. The mixture was centrifuged at 2000 rpm for 20 min, and the suspension was collected and centrifuged at 8000 rpm for 5 min to precipitate the multilayer MoS_2 as a precursor for the next step. Then, the as-synthezised BiOBr microspheres and multilayer MoS_2 with different weight ratios were added to 50 mL NMP for a further LPE with 9 h of tip-sonication to obtain heterojunctions with different weight ratio of MoS_2 and BiOBr (see Table S1 for details). After centrifuging the mixture at 2000 rpm for 20 min, stable colloidal suspensions were obtained. Then, ethanol and H_2O were added to precipitate the products.

4.3 Characterization

P-XRD was performed on a Panalytical X'Pert PRO diffractometer by using a Cu Kα source (40 kV, 40 mA). The Raman spectra were taken using a Senterra spectrometer from Bruker Optics with OPUS 7.5 software. The wavelength of the excitation laser was 532 nm. The concentrated samples were drop casted on the glass and measured with 80 co-addition and 25 seconds integration time. SEM was conducted on a Carl Zeiss electron microscope with an acceleration voltage of 3 kV and current of 100 pA. EDX was performed with a detector from Oxford Instruments (X-Max 50) with an acceleration voltage of 15 keV and current of 2 nA. The working distance is 5 mm. XPS spectra were recorded on a spectroscopy from Physical Electronics GmbH (PHI 5000 VersaProbe II). Bright-filed TEM (BF-TEM) imaging was carried out on a JEOLJEM-1011 instrument with an acceleration voltage of 100 kV. The samples were prepared by dropping dilute suspensions of the nanomaterials in ethanol onto carbon film-coated 200 mesh copper grids. HRTEM HAADF-STEM images and STEM-EDX analyses were carried out on an image-Cs-corrected JEOL JEM-2200FS TEM equipped with a Bruker X-Flash 5060 SDD, operated at 200 kV. For these analyses, holey-amorphous carbon films on Cu grids were used as supports. HRTEM images presented here have been acquired using a direct-electron-detection camera (K2 Summit, Gatan), so as to reduce the electron dose rate, thus beam damage. .The STEM-EDX elemental maps presented here were obtained by integration of raw spectra in the regions of Bi Lα and Mo Kα peaks.

4.4 Electrochemical and photoelectrochemical measurements

EC and PEC HER tests were performed using a photoelectrochemical reaction cell with three electrodes in a 0.5 M Na_2SO_4 eletrolytic medium. The reference electrode is Ag/AgCl (saturated KCl electrolyte) and the counter electrode is a platinum wire. For the PEC HER experiments, all the samples were dried in air and disperse again in ethanol with a concentration of 5 mg/mL, and the inks were drop casted on conductive FTO glass. A mercury lamp with a light intensity of 16 mW/cm² was used as a light source. The potentiostatic test was conducted on an Autolab instrument, and the LSV was performed at a scan rate of 10 mV/s in the range of 0.2~-0.6 V vs. RHE. The transient photocurrent measurements were examined at open circuit voltage during four on/off light cycles.

4.5 Computational details

To avoid the deformation of the electronic structure of the interface, BiOBr was considered within a 5x5 supercell and MoS_2 with a 6x6 supercell, leading to a final cell size of 1.9 x 1.9 x 3 nm (void was added to the z direction to avoid spurious interactions). In this way, the obtained supercell has a minimal lattice mismatch ratio of 1.58% between the two different cells. The choice of the weight percentage has been dictated by the high computational cost due to the presence of multilayers of BiOBr interacting with MoS_2 for 1% and 5% MoS_2/BiOBr HJs (50 and 9 BiOBr layers are required, respectively. See SI for additional information). Hence, three representative interfaces with 18, 30 and 50% MoS_2/BiOBr were chosen.

The geometry optimization of the three interfaces was performed using the PBE-D3 functional with the VASP software.[53–58] We used a plane wave basis set with an energy cutoff of 500 eV. The geometry optimization criteria were set to 10^{-5} eV for energy and to 0.02 eV/Å for forces on each atom. The calculations were performed at the Γ K-point, and a Gaussian smearing of 0.03 eV was applied for the whole calculations

Author Contributions

M.W. and T. G. conceived the initial idea for this research. M. W. performed the synthesis, XRD, Raman spectra, SEM-EDX, PEC experiments, analysed the data and wrote the manuscript. S. O. performed the computational simulation. Z. L. performed BF-TEM imaging and R.B. carried out HRTEM and STEM analyses. M. C. provided valuable suggestions in the synthesis and performed part of the Raman measurements. M. Ca., J. G. and M. C. performed XPS measurement and analysed the data. All authors contributed to manuscript writing and revision.

Conflicts of interest

The authors declare that they have no known competing financial interests or personal relationships that could have appeared to influence the work reported in this paper.

Acknowledgements

M.W. and T.G. are grateful for the financial support from the Hessisches Ministerium für Wissenschaft und Kunst (HMWK) through the programme Marie Skłodowska-Curie-Stipendium Hessen. T. G. also acknowledges the support of the European Commission through the H2020 FET-PROACTIVE-EIC-07-2020 project LIGHT-CAP (grant agreement No. [101017821]) and of the European Research Council through the ERC StG project JANUS BI (grant agreement No. [101041229]). We thank Fabian Schmitz for help with the PEC measurements.

Notes and references

1 H. Yang, K. Dai, J. Zhang and G. Dawson, *Chinese J. Catal.*, 2022, **43**, 2111–2140.

2 I. V. Bagal, N. R. Chodankar, M. A. Hassan, A. Waseem, M. A. Johar, D. H. Kim and S. W. Ryu, *Int. J. Hydrogen Energy*, 2019, **44**, 21351–21378.

3 M. Tayebi and B. K. Lee, *Renew. Sustain. Energy Rev.*, 2019, **111**, 332–343.

4 P. Sharma, J. W. Jang and J. S. Lee, *ChemCatChem*, 2019, **11**, 157–179.

5 S. Chen, T. Liu, Z. Zheng, M. Ishaq, G. Liang, P. Fan, T. Chen and J. Tang, *J. Energy Chem.*, 2022, **67**, 508–523.

6 K. C. Kwon, S. Choi, K. Hong, C. W. Moon, Y. S. Shim, D. H. Kim, T. Kim, W. Sohn, J. M. Jeon, C. H. Lee, K. T. Nam, S. Han, S. Y. Kim and H. W. Jang, *Energy Environ. Sci.*, 2016, **9**, 2240–2248.

7 R. Pan, J. Liu, Y. Li, X. Li, E. Zhang, Q. Di, M. Su and J. Zhang, *J. Mater. Chem. A*, 2019, **7**, 23038–23045.

8 X. Li, Z. Wang, J. Zhang, K. Dai, K. Fan and G. Dawson, *Mater. Today Phys.*, 2022, **26**, 100729.

9 S. Wu and Y. H. Hu, *Chem. Eng. J.*, 2021, **409**, 127739.

10 S. Chen, D. Huang, P. Xu, W. Xue, L. Lei, M. Cheng, R. Wang, X. Liu and R. Deng, *J. Mater. Chem. A*, 2020, **8**, 2286–2322.

11 C. Y. Toe, J. Scott, R. Amal and Y. H. Ng, *J. Photochem. Photobiol. C Photochem. Rev.*, 2019, **40**, 191–211.

12 M. Wang, Z. Dang, M. Prato, U. Petralanda, I. Infante, D. V Shinde, L. De Trizio and L. Manna, , DOI:10.1021/acsanm.9b01205.

13 C. W. Siao, H. L. Chen, L. W. Chen, J. L. Chang, T. W. Yeh and C. C. Chen, *J. Colloid Interface Sci.*, 2018, **526**, 322–336.

14 H. Lei, H. Zhang, Y. Zou, X. Dong, Y. Jia and F. Wang, *J. Alloys Compd.*, 2019, **809**, 151840.

15 Z. Ai, W. Ho, S. Lee and L. Zhang, *Environ. Sci. Technol.*, 2009, **43**, 4143–4150.

16 J. Di, C. Chen, C. Zhu, P. Song, J. Xiong, M. Ji, J. Zhou, Q. Fu, M. Xu, W. Hao, J. Xia, S. Li, H. Li and Z. Liu, *ACS Appl. Mater. Interfaces*, 2019, **11**, 30786–30792.

17 X. Xue, R. Chen, H. Chen, Y. Hu, Q. Ding, Z. Liu, L. Ma, G. Zhu, W. Zhang, Q. Yu, J. Liu, J. Ma and Z. Jin, *Nano Lett.*, 2018, **18**, 7372–7377.

18 M. Shi, G. Li, J. Li, X. Jin, X. Tao, B. Zeng, E. A. Pidko, R. Li, C. Li, M. Shi, X. P. Tao, B. Zeng, R. G. Li, C. Li, J. M. Li, X. Jin, G. N. Li and E. A. Pidko, *Angew. Chemie*, 2020, **132**, 6652–6657.

19 S. S. M. Bhat and H. W. Jang, *ChemSusChem*, 2017, **10**, 3001–3018.

20 X. Wang, Z. Chen, J. Zheng, Y. Li, X. Peng, X. Zhang, H. Yin, X. Xiong, J. Duan, X. Li, Z. Wang, Z. Chen, J. Han, W. Xiao and Y. Yao, *ACS Appl. Energy Mater.*, 2020, **3**, 11848–11854.

21 X. Li, Q. Liu, F. Deng, J. Huang, L. Han, C. He, Z. Chen, Y. Luo and Y. Zhu, *Appl. Catal. B Environ.*, 2022, **314**, 121502.

22 H. Yang, J. feng Zhang and K. Dai, *Chinese J. Catal.*, 2022, **43**, 255–264.

23 J. Zhang, J. Fu and K. Dai, *J. Mater. Sci. Technol.*, 2022, **116**, 192–198.

24 W. Xia, L. Dai, P. Yu, X. Tong, W. Song, G. Zhang and Z. Wang, *Nanoscale*, 2017, **9**, 4324–4365.

25 Y. Deng, Z. Luo, N. J. Conrad, H. Liu, Y. Gong, S. Najmaei, P. M. Ajayan, J. Lou, X. Xu and P. D. Ye, *ACS Nano*, 2014, **8**, 8292–8299.

26 H. Tabata, Y. Sato, K. Oi, O. Kubo and M. Katayama, *ACS Appl. Mater. Interfaces*, 2018, **10**, 38387–38393.

27 G. Hyuk Shin, C. Park, K. June Lee, H. Jun Jin and S.-Y. Choi, , DOI:10.1021/acs.nanolett.0c01460.

28 R. Long and O. V Prezhdo, *Nano Lett*, 2016, **16**, 42.

29 W. Yin, X. Cao, B. Wang, Q. Jiang, Z. Chen and J. Xia, *ChemistrySelect*, 2021, **6**, 928–936.

30 Y. Li, Z. Lai, Z. Huang, H. Wang, C. Zhao, G. Ruan and F. Du, *Appl. Surf. Sci.*, 2021, **550**, 149342.

31 B. Zhang, M. Zhang, L. Zhang, P. A. Bingham, M. Tanaka, W. Li and S. Kubuki, *J. Colloid Interface Sci.*, 2021, **594**, 635–649.

32 H. Yu, H. Huang, K. Xu, W. Hao, Y. Guo, S. Wang, X. Shen, S. Pan and Y. Zhang, *ACS Sustain. Chem. Eng.*, 2017, **5**, 10499–10508.

33 P. Intaphong, A. Phuruangrat, · K Karthik, · Phattranit Dumrongrojthanath, T. Thongtem and S. Thongtem, *J. Inorg. Organomet. Polym. Mater.*, 1234, **30**, 714–721.

34 H. Li, Q. Zhang, C. C. R. Yap, B. K. Tay, T. H. T. Edwin, A. Olivier and D. Baillargeat, *Adv. Funct. Mater.*, 2012, **22**, 1385–1390.

35 B. P. Majee, S. Mishra, R. K. Pandey, R. Prakash and A. K. Mishra, *J. Phys. Chem. C*, 2019, **123**, 18071–18078.

36 S. Maulik, S. Basu, K. Kanakamedala and T. Daniels-Race, *J. Electron. Mater. 2019 486*, 2019, **48**, 3451–3458.

37 J. Tang, Z. Wei, Q. Wang, Y. Wang, B. Han, X. Li, B. Huang, M. Liao, J. Liu, N. Li, Y. Zhao, C. Shen, Y. Guo, X. Bai, P. Gao, W. Yang, L. Chen, K. Wu, R. Yang, D. Shi, G. Zhang, J. Tang, Z. Wei, Q. Wang, Y. Wang, X. Li, B. Huang, M. Liao, J. Liu, N. Li, Y. Zhao, C. Shen, Y. Guo, X. Bai, W. Yang, L. Chen, K. Wu, R. Yang, D. Shi, G. Zhang, B. Han and P. Gao, *Small*, 2020, **16**, 2004276.

38 D. Yang, C. Lu, J. Ma, M. Luo, Q. Zhao, Y. Jin and X. Xu, *Appl. Surf. Sci.*, 2021, **538**, 147989.

39 Y. Li, H. Jiang, X. Wang, X. Hong and B. Liang, *RSC Adv.*, 2021, **11**, 26855–26875.

40 C. V. Nguyen, N. N. Hieu and D. T. Nguyen, *Nanoscale Res. Lett.*, 2015, **10**, 1–8.

41 M. Barhoumi and M. Said, *Optik (Stuttg).*, 2020, **216**, 164631.

42 Q. Fan, X. Chen, L. Wei, K. Yang and C. Yu, *Opt. Mater. (Amst).*, 2020, **109**, 110316.

43 H. Tian, R. Cheng, M. Lin, P. Li, Y. Lv and S. Ran, *Inorg. Chem. Commun.*, 2020, **118**, 108018.

44 J. Han, Y. Gao, Y. Li, Z. Chen, X. Liu, X. Xiong, X. Zhang, Y. Jiang, Q. Luo, Y. Song, Z. Wang, X. Li, Z. Chen and W. Xiao, *J. Phys. Chem. C*, 2020, **124**, 24164–24170.

45 D. M. Kabtamu, G.-Y. Lin, Y.-C. Chang, H.-Y. Chen, H.-C. Huang, N.-Y. Hsu, Y.-S. Chou, H.-J. Wei and C.-H. Wang, , DOI:10.1039/c7ra12926b.

46 F. Chang, C. Li, J. Chen, J. Wang, J. Luo, Y. Xie, B. Deng and X. Hu, *Superlattices Microstruct.*, 2014, **76**, 90–104.

47 C. Zhao, Y. Liang, W. Li, X. Chen, Y. Tian, D. Yin and Q. Zhang, *J. Mater. Sci. Mater. Electron.*, 2020, **31**, 1868–1878.

48 M. Hojamberdiev, G. Zhu, H. Lu, M. Kumar, M. Wang and J. Gao, *J. Mater. Sci. Mater. Electron.*, 2019, **30**, 2610–2621.

49 K. Wu, Z. Qin, X. Zhang, R. Guo, X. Ren and X. Pu, *J. Mater. Sci.*, 2020, **55**, 4017–4029.

50 J. Wang, Y. Zhang, L. Tian, F. Liu and Q. Xia, *J. Nanoparticle Res.*, 2014, **16**, 1–10.

51 C. Yue, C. Li, P. Zhang, M. Fan, A. Haryono, Y. Leng, Y. Dong and P. Jiang, *New J. Chem.*, 2021, **45**, 12938–12944.

52 X. Shi, X. Chen, X. Chen, S. Zhou, S. Lou, Y. Wang and L. Yuan, *Chem. Eng. J.*, 2013, **222**, 120–127.

53 S. Grimme, J. Antony, S. Ehrlich and H. Krieg, *J. Chem. Phys.*, 2010, **132**, 154104.

54 G. Kresse and J. Furthmüller, *Comput. Mater. Sci.*, 1996, **6**, 15–50.

55 G. Kresse and J. Hafner, *Phys. Rev. B*, 1994, **49**, 14251.

56 G. Kresse and J. Furthmüller, *Phys. Rev. B*, 1996, **54**, 11169.

57 G. Kresse and J. Hafner, *Phys. Rev. B*, 1993, **47**, 558.

58 P. E. Blöchl, *Phys. Rev. B*, 1994, **50**, 17953.